Heliyon 9 (2023) e20520

Contents lists available at ScienceDirect

Heliyon

journal homepage: www.cell.com/heliyon

Clay-based 1D-2D halloysite&g-C_3N_4 nanostructured meat floss for photocatalytic hydrogen evolution

Sen Lin [a,b,*], Shiyong Sun [a,b,**], Zhengwei Li [a]

[a] Key Laboratory of Solid Waste Treatment and Resource Recycle of Ministry of Education, School of Environment and Resource, Southwest University of Science and Technology, Mianyang, Sichuan, 621010, PR China
[b] Key Laboratory of Non-metallic Mineral Geology and Utilization in Sichuan Provincial Higher Education Institutions, Southwest University of Science and Technology, Mianyang, Sichuan, 621010, PR China

ARTICLE INFO

Keywords:
G-C_3N_4
Halloysite
Cell pulverizing
Electrostatic self-assembly
H_2 evolution

ABSTRACT

Graphitic carbon nitride (g-C_3N_4) has drawn extensive attention with some features including visible-light response as non-metallic semiconductor, low cost in raw material and green pollution-free for environment, but suffers from some issues such as fast charge carriers' recombination, easy aggregation, etc. In this work, the 1D-2D HNTs&g–C_3N_4–X binary materials similar to *meat floss* pattern in a series of halloysite loading amounts are designed *via* a facile electrostatic self-assembly strategy with debris g-C_3N_4 after cell pulverizing treatment and HNTs that outwardly modified by cetyltrimethylammonium bromide (CTAB) as the building blocks. The halloysite-mediated satellite-core material displays a photocatalytic of H_2 evolution performance with the highest evolution rate of 137.0 μmol g^{-1} h^{-1} in visible light condition with no co-catalysts, and is ~3.4 times that of bulk g-C_3N_4, mainly benefiting from the reduced nanometer size of debris g-C_3N_4 and enhanced interface dispersion ability by HNTs, resulting in ameliorative separation efficiency of photogenerated charge carriers. This research conclusively provides the new perspective towards the performance enhancement of water splitting of g-C_3N_4 in raw clay mineral modification mode and broadens the applications of mineral-based composite in the renewable energy utilization field.

1. Introduction

The modern economy development is inseparable from exploitation and utilization of energy, whereas the excessive consumption of the fossil fuels like coal, oil and natural gas has exacerbated the energy crisis in past decades, accompanied by the increasingly fierce environmental deterioration issues, which in turn hinders the sustainable social and economic development. In this manner, people are gradually focusing on the research and utilization of green energy technologies. Photocatalysis is a kind of technology that can convert solar energy into chemical energy, in which hydrogen (H_2) production from photocatalytic water splitting under simulated external sunlight by semiconductors, is regarded as a prospective conversion due to the advantages of direct energy source, mild process and

* Corresponding author. Key Laboratory of Solid Waste Treatment and Resource Recycle of Ministry of Education, School of Environment and Resource, Southwest University of Science and Technology, Mianyang, Sichuan, 621010, PR China.
** Corresponding author. Key Laboratory of Solid Waste Treatment and Resource Recycle of Ministry of Education, School of Environment and Resource, Southwest University of Science and Technology, Mianyang, Sichuan, 621010, PR China.
E-mail addresses: lsen@swust.edu.cn (S. Lin), shysun@swust.edu.cn (S. Sun).

https://doi.org/10.1016/j.heliyon.2023.e20520
Received 12 June 2023; Received in revised form 21 September 2023; Accepted 27 September 2023
Available online 28 September 2023

pollution-free [1]. Particularly, H_2 has the highest energy density value (120 MJ kg^{-1}), and the product after combustion is only water without any environmental pollution, which is expected to alleviate energy depletion and environmental deterioration problems [2–4]. For photocatalytic water splitting hierarchy, it is a crucial part for design and development of semiconductors with suitable bandgaps. To date, a variety of typical semiconductor-based materials like TiO_2 [5–7], ZnO [8], CdS [9,10], $BiVO_4$ [11], $Bi_4Ti_3O_{12}$ [12, 13], black phosphorous [14], and g-C_3N_4 [15–19] have been explored for the applications such as H_2 evolution, water oxidation, CO_2 reduction, environmental purification, etc. As a polymeric metal-free semiconductor, the g-C_3N_4 is exemplified to be a kind of ideal alternative in terms of its suitable band position, thermal stability and facile synthesis route. Meanwhile, the g-C_3N_4 with bulk pattern is always suffered from some inherent drawbacks, including the easy recombination of charges, limited active sites and limited visible-light adsorption [20], though several strategies such as surface modification [20–22], heterojunction construction [23–28], foreign element doping [28–30], etc., are conducted to ameliorate its photocatalytic activity, the complex operation and costly synthesis status still impede its large-scale industrialization.

Recently, it is discovered that hybrid synthesis *via* the combination of photocatalysts and natural clay minerals which possess good adsorption, chemical stability and excellent specific surface area, has shown the effect of significantly improving photocatalytic properties of materials. Shu et al. loaded the polymeric carbon nitride (PCN) onto the surface of metakaolin by vapor deposition route to get the mineral-based composite, it was found that the H_2 evolution performance of this compound is 3.8-fold that of pristine g-C_3N_4, owing to the nanoscale of PCN and electronegativity of metakaolin [31]. The bentonite-mediated WO_3/g-C_3N_4 nanosheet (2D-WBCN) was constructed to evaluate the property of selective photocatalytic CO_2 reduction to CH_4 with H_2O as reducing agent, and the as-prepared 2D-WBCN showed the best performance for CH_4 production in visible light irradiation, which was 6.01, 6.76 and 25.30-folds over those of WO_3/g-C_3N_4, Bt/g-C_3N_4 and g-C_3N_4, respectively, its enhanced CO_2 reduction capability can be attributed to the Z-scheme effect between WO_3 and g-C_3N_4, coupling with bentonite as electron moderator [32]. Sun et al. encapsulated TiO_2 nanoparticles into the mineral-based microcapsules with montmorillonite as building blocks, the methylene blue and rhodamine B degradation efficiencies were obviously improved for this constructed colloidosomes compared with pristine TiO_2, due to the steric hindrance effect of montmorillonite which as the assembly membrane of colloidosomes, to endow inner TiO_2 a higher photocatalytic activity [5]. Through a facile hydrolysis way, the BiOCl/diatomite material was synthesized to inspect the removal efficiency of ciprofloxacin (CIP), the experiment revealed that BIOCl combined with diatomite which accounts for 60% of the total mass has 94% removal efficiency to CIP, the total organic carbon reached 42.9% within 240 min, the diatomite can act as the carrier to evenly immobilize BIOCl on its surface, preventing the aggregation of BIOCl and further making BIOCl expose more reaction active sites, thus promoting charges' separation and migration efficiency [33]. Dong et al. embed celestite particles into defective g-C_3N_4 with the existence of N vacancies, it was shown that the NO removal efficiency activity of the composite under visible light illumination is elevated 3.8 times compared with g-C_3N_4, for the synergistic function of celestite plays as the electronic media and N vacancies capture the photoinduced electrons [34]. Inspiringly, all these reported researches above provide directions for exploring the improvement of photocatalytic properties of photocatalysts with the regulation of abundant minerals.

Halloysite belongs to aluminosilicate mineral, it has a hollow tubular micromorphology, which is known as halloysite nanotubes (HNTs). The molecular formula of HNTs is $Al_2(OH)_4Si_2O_5{\cdot}nH_2O$, and the chemical composition is the same as kaolin, the inner and outer surface of HNTs severally has positive and negative charges, coupled with tubular architecture, endowing HNTs good adsorbability, dispersity and biocompatibility [35]. At the same time, due to large surface area, HNTs would offer lots of adsorption sites when combined with photocatalysts as the high-quality solid carrier, thereby improving the photocatalytic activity of materials. To achieve a simple loading for ZnO, Massaro et al. prepared a ZnO@HNTs hybrid with HNTs as superficial support for ZnO through a one-pot method, the study found that the loading effect from HNTs can enhance light absorption property ZnO, effectively realizing methylene blue and rhodamine B treatments, the degradation efficiency for methylene blue after eight cycles did not significantly change, the result of reactive radical trapping experiment illustrated that h^+ and OH are main active substances in this reaction process [36]. Huang et al. prepared $Cd_{0.5}Zn_{0.5}S$@HNTs in water bath, the HNTs were grafted and modified using sodium chloride, potassium iodide, disodium ethylenediaminetetraacetate (EDTA), etc., to survey the effects of $Cd_{0.5}Zn_{0.5}S$ nanospheres loading and superficial modification on the photocatalytic of H_2 evolution by materials, and it was presented that the dispersion of HNTs to $Cd_{0.5}Zn_{0.5}S$, combining with h^+ trapping function from EDTA, which jointly promoting H_2 production performance, the maximum rate reached 25.67 mmol g^{-1} h^{-1}, and was 7.03 times of pure $Cd_{0.5}Zn_{0.5}S$ [37]. In addition to the outer tube's surface, the inner cavity of HNTs can also be applied as loading site, Vinokurov et al. successfully produced CdS nanoparticles into the outer and inner lumens of HNTs with the utilization of Schiff-based ligand to overcome the charge's repulsion between HNTs and CdS, the as-constructed CdS/HNTs showed an outstanding rate of 20 mmol g^{-1} h^{-1} without any co-catalysts [38]. In the research of polybasic mineral-based compound, Wang et al. wrapped Au nanoparticles, CdS and g-C_3N_4 onto the surface of HNTs to build a HNTs/Au/CdS/g-C_3N_4 quaternary heterojunction (HCAC), and it was discovered that CO and CH_4 yields are severally 55.4 and 8.6 μmol g^{-1} in the photocatalytic of CO_2 reduction test of HCAC-3, which was 5-fold over that of HNTs/g-C_3N_4, while the ratio of photo-degradation to tetracycline reached 87.4% within 120 min, which was enhanced about 2.2 times compared with HNTs/g-C_3N_4, the improved property is relevant to type-II heterojunction between CdS and g-C_3N_4, as well as the LSPR effect of Au nanoparticles [39]. Therefore, HNTs have the benefits of improving the performances of the photocatalytic materials, including the fields of environmental purification, new energy conversion, etc.

Herein, the debris g-C_3N_4 is firstly attempted to fabricate by cell pulverizing treatment, then combined with HNTs that is modified by CTAB as the assembly substrates to obtain a 1D-2D nanocomposite which is similar to *meat floss* (denoted as HNTs&g-C_3N_4) by electrostatic self-assembly strategy. In virtue of the elevated separation and migration efficiency of charges' carriers of g-C_3N_4 and surface dispersion effect from HNTs, the optimal H_2 production rate of as-prepared materials is 137.0 μmol g^{-1} h^{-1} with no co-catalysts, and is 3.4 times over g-C_3N_4. This research offers a new structural design thinking for mineral-based photocatalysts towards the new energy application fields.

2. Experimental section

2.1. Materials

The halloysite nanotubes (HNTs) were purchased from Hubei, Shiyan, China, cetyltrimethylammonium bromide (CTAB) was obtained from Guangzhou Sharp Technology Co., Ltd, melamine was provided in Shanghai Maclin Biochemical Technology Co., Ltd, methanol, sal mirabile, lactic acid and alcohol were offered from Chengdu Cologne Chemical Co., Ltd, ultrapure water was used for all solutions, the chemical reagents were analytically pure and directly used with no purification treatment.

2.2. Synthesis of samples

The g-C_3N_4 with bulk phase was fabricated by calcination with melamine as precursor, 5 g of melamine was calcined with a temperature of 520 °C in 4 h, at a heating rate of 3 °C/min. The 0.5 g of bulk g-C_3N_4 was dissolved in 300 mL of mixed solution ($V_{methanol}$:V_{water} = 1:1) and crushed by cell pulverizing, the sample was crushed for 7 h and centrifuged at 5000 r/min after reaction to prepare the debris g-C_3N_4 (denoted as 2D-g-C_3N_4). The reagent with HNTs and CTAB mass ratio of 10:1 was carried out for the modified reaction at 80 °C for 12 h, the sample was centrifuged at 5000 r/min and washed several times to obtain modified HNTs (denoted as HNTs-C). Based on the electrostatic self-assembly strategy, in 30 mL of deionized water, 2D-g-C_3N_4 and HNTs with series of mass percentages (5%, 10%, 20%, 50%, 100%) were reacted for 8 h at room temperature, after the reaction, the products were collected and centrifuged at 5000 r/min to collect the products. The HNTs/2D-g-C_3N_4 compound with different mass fractions of HNTs are marked as HNTs&g–C_3N_4–X (X = 1, 2, 3, 4, 5).

2.3. Characterizations

The X-ray diffractometer (XRD, Bruker, DE) was tested by D8 Advance diffractometer with Cu K_α radiation (λ = 1.5178 Å) from 3° to 80°. The grain size and zeta potential were analyzed by a zeta potential analyzer (Microtrac, USA). The Fourier transform infrared (FTIR, PerkinElmer, USA) spectra were collected through spectrometric analyzer over wavenumber from 4000 to 400 cm^{-1}. The elemental compositions and information were characterized by X-ray photoelectron spectroscopy (XPS, Thermp Fisher, UK) instrument. The dimension, morphology and relevant elemental detection were investigated through the atomic force microscopy (AFM, Bruker, DE), scanning electron microscope (SEM, Hitachi, JPN) and transmission electron microscopy (TEM, Zeiss, DE). The UV–Vis absorption intensity was characterized with diffuse reflectance spectrophotometer (DRS, Shimadzu, JPN) with $BaSO_4$ as reference powder. The photoluminescence (PL, Hitachi, JPN) emission spectra were determined through a fluorescence system by a xenon lamp.

2.4. Photoelectrochemical measurements

The transient photocurrent and electrochemical impedance spectra were implemented through the electrochemical workstation (Chenhua Instrument Co., Ltd, Shanghai, China). For working electrode, 10 mg of sample was dispersed into the alcohol and ultrasound for 15 min, the slurry was then daubed on the surface of indium tin oxide (ITO) substrate, and dried at 120 °C for 8 h. During the test, the solution containing 0.1 M Na_2SO_4 was selected as the electrolyte with xenon lamp as visible light source (a 420 nm UV cut-off filter was employed).

2.5. H_2 evolution characterizations

The H_2 evolution experiments were carried out with an off-line H_2 production glass device. The 50 mg of corresponding materials were suspended into 90 mL of deionized water with 10 mL of lactic acid as sacrificial agent, the solution was evacuated through the vacuum pump for 20 min to remove excess air of glass reactor to keep an anaerobic environment, a 300 W xenon lamp (Perfectlight Technology Co., Ltd, Shanghai, China) was used as the visible light source (λ ≥ 420 nm). At an interval of every 1 h, 1 mL of target gas was extracted from the reaction glassware by sampling needle and analyzed by a gas chromatography (Timei Scientific Instrument Co., Ltd, Shanghai, China).

The apparent quantum efficiency (AQE) of HNTs&g–C_3N_4–2 was tested with a series of band-pass filters (420, 450, 500, 550 and 600 nm). The irradiated surface area and peak width of the entire band-pass filters were 30 cm^2 and 15 nm, respectively. The corresponding formula of AQE is as follows:

$$AQE = \frac{Number\ of\ generated\ hydrogen \times 2}{Number\ of\ incident\ photons} \times 100\% = \frac{2 \times n_{H_2} \times N_A}{PS\lambda/hc} \times 100\%$$

3. Results and discussion

3.1. Structure and morphology characterizations

Fig. 1 shows the preparation route of halloysite-based mineral composite with 1D-2D architecture. For g-C_3N_4, after the annealing at 520 °C and further cell pulverizing treatment, the colour of sample's powder became lighter than bulk g-C_3N_4 (Figs. S1a and b), the

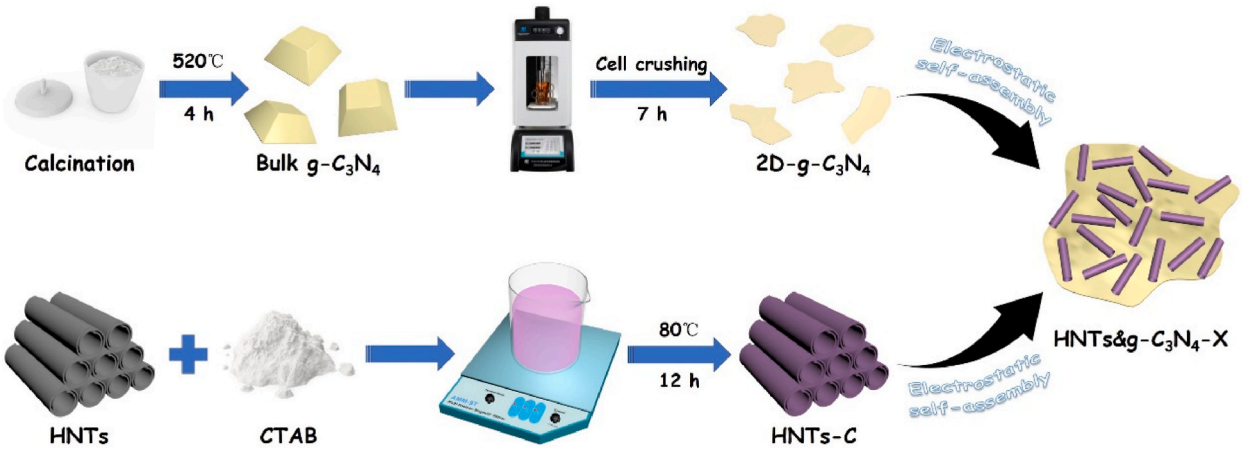

Fig. 1. Schematic diagram of 1D-2D HNTs&g–C_3N_4–X composite synthesis.

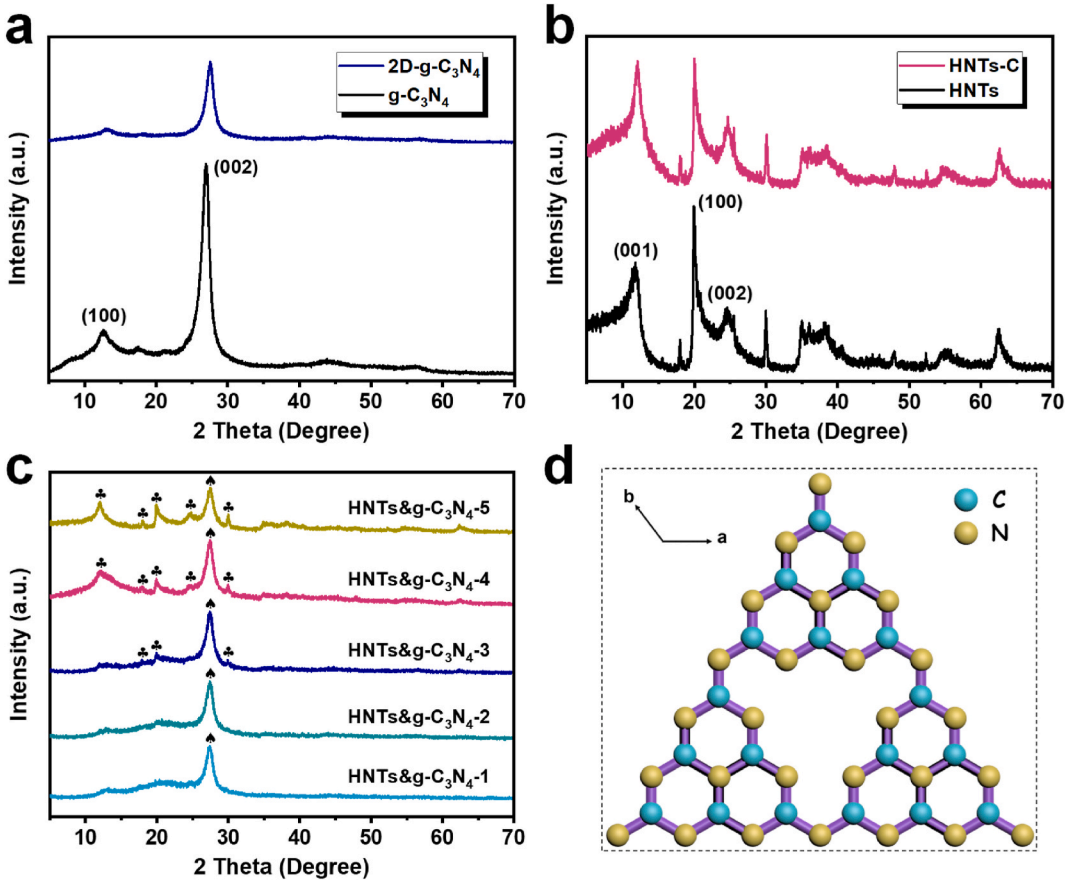

Fig. 2. XRD patterns of g-C_3N_4 and 2D-g-C_3N_4 (a), HNTs and HNTs-C (b) and HNTs&g–C_3N_4–X (c). The diagram of g-C_3N_4 crystal mode (d).

2D-g-C_3N_4 exhibited a better solution dispersion nature and had obvious Tyndall effect in aqueous phase compared to bulk g-C_3N_4 (Figs. S1c and d), indicating the g-C_3N_4 physical size has been significantly changed after this management [20]. For HNTs, the colour of the sample did not change before and after modification by CTAB (Fig. S2), while the zeta potential values of g-C_3N_4, 2D-g-C_3N_4, HNTs and HNTs-C in aqueous solution were tested to be −20.4, −19.8, −4.7 and 16.1 mV, respectively (Fig. S3), demonstrating that the surface of HNTs is positively charged after superficial modification, being combined with 2D-g-C_3N_4 to acquire 1D-2D compound through electrostatic self-assembly technique (Fig. S4).

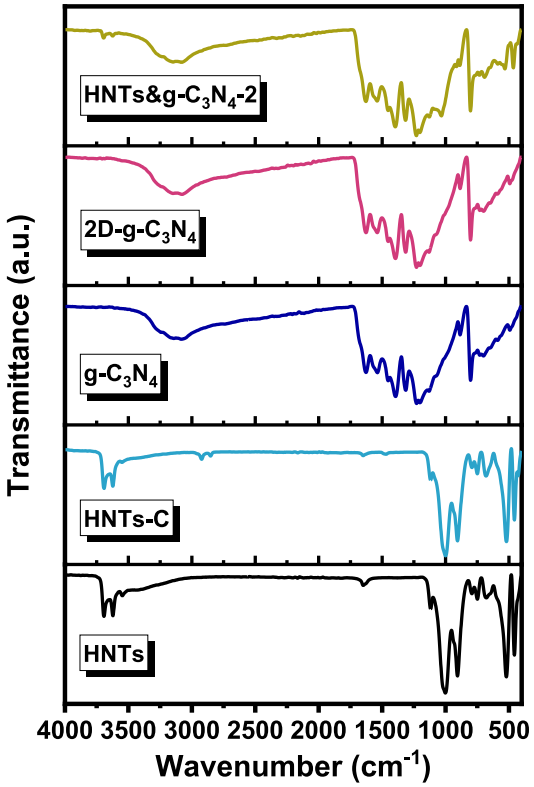

Fig. 3. FTIR spectra of HNTs, HNTs-C, g-C_3N_4, 2D-g-C_3N_4 and HNTs&g–C_3N_4–2.

The crystalline information of as-synthesized materials was evaluated by XRD patterns. As observed from Fig. 2a, the characteristic diffraction peaks located at approximately 13° and 26.7° are readily assigned to (100) lattice plane and (002) interlayer diffraction of g-C_3N_4, which should be denoted to its in-plane structural stacking of multiple tir-*s*-triazine rings and inter-planar structural stacking of aromatic ring system [15,24], respectively (Fig. 2d). After cell pulverizing treatment, the feature reflection positions at crystal planes of (100) and (002) of 2D-g-C_3N_4 are all shifted to higher degree compared to bulk g-C_3N_4, and the intensity of diffraction peaks is simultaneously become weaker, implying that bulk g-C_3N_4 would be decomposed into debris forms through the mechanical force from cell pulverizing, the van der Waals force between the layers of g-C_3N_4 is weakened and the hydrogen bond is destroyed, which in turn damaging the interlayer stacking structure and enlarging the interlayer spacing of g-C_3N_4 [20]. As displayed from Fig. 2b, the main diffraction peaks positions of HNTs has not been obviously changed after the grafting modification by CTAB, illustrating the crystalline phase structure of HNTs is remained stable [37]. As shown in Fig. 2c, the relevant peaks for a series of HNTs&g–C_3N_4–X hybrid are consistent with individual component containing HNTs and 2D-g-C_3N_4 with no other characteristic reflections, and the peaks' intensity belonging to 2D-g-C_3N_4 would be decreased with the increased mass percentage of HNTs within fabricated hybrid, indicating that HNTs are successfully combined with g-C_3N_4 fragments.

The internal FTIR structural information about pure HNTs, modified HNTs, bulk phase g-C_3N_4, debris g-C_3N_4 and corresponding hybrid was characterized. In Fig. 3, the bands located at 3692.8 and 3621.9 cm^{-1} for HNTs are well indexed to stretching vibration peaks of O–H, a typical antisymmetric stretching vibration mode of Si–O–Si and in-plane bending vibration mode of Al–OH are detected at 1001.1 and 906.3 cm^{-1}, respectively. After the superficial grafting by CTAB, three new functional group peaks emerged at 2922.8, 2852.4 and 1469.7 cm^{-1} that are severally belonged to antisymmetric stretching vibration, symmetric stretching vibration and variant angle vibration from $–CH_2$ [10]. The 3000∼3500 cm^{-1} broad bands for g-C_3N_4 should be originated from the stretching vibration peaks of –NH and the hydroxyl of internal water molecules, the several absorption bands presented in 1200∼1650 cm^{-1} region are credited to prominent stretching vibration peaks of aromatic C–N and C═N bonds, whereas the intense peak appeared at 802.5 cm^{-1} is derived from out-of-plane bending mode of characteristic tir-*s*-triazine rings compositions derived from g-C_3N_4 interlayers [15], and there is no palpable change of FTIR spectra for 2D-g-C_3N_4 compared to bulk g-C_3N_4, confirming that such cell pulverizing handle only provide physical smash and didn't disrupt the molecular structures of g-C_3N_4. All detected bands of HNTs&g–C_3N_4–2 resemble those from HNTs and g-C_3N_4 with no other impurity modes, signifying that HNTs is successfully combined with debris g-C_3N_4 by the electrostatic self-assembly principle and these structural groups have been remained intact after electrostatic self-assembly procedure between raw materials [6,10,37]. The corresponding wavenumber information is listed in Table S1.

The elemental chemical states of HNTs-C, 2D-g-C_3N_4 and HNTs&g–C_3N_4–2 were illustrated through XPS. As displayed from Fig. 4a, the survey spectrum for HNTs&g–C_3N_4–2 hybrid illustrates the existence of O, N, C, Si and Al elements, further affirming combination

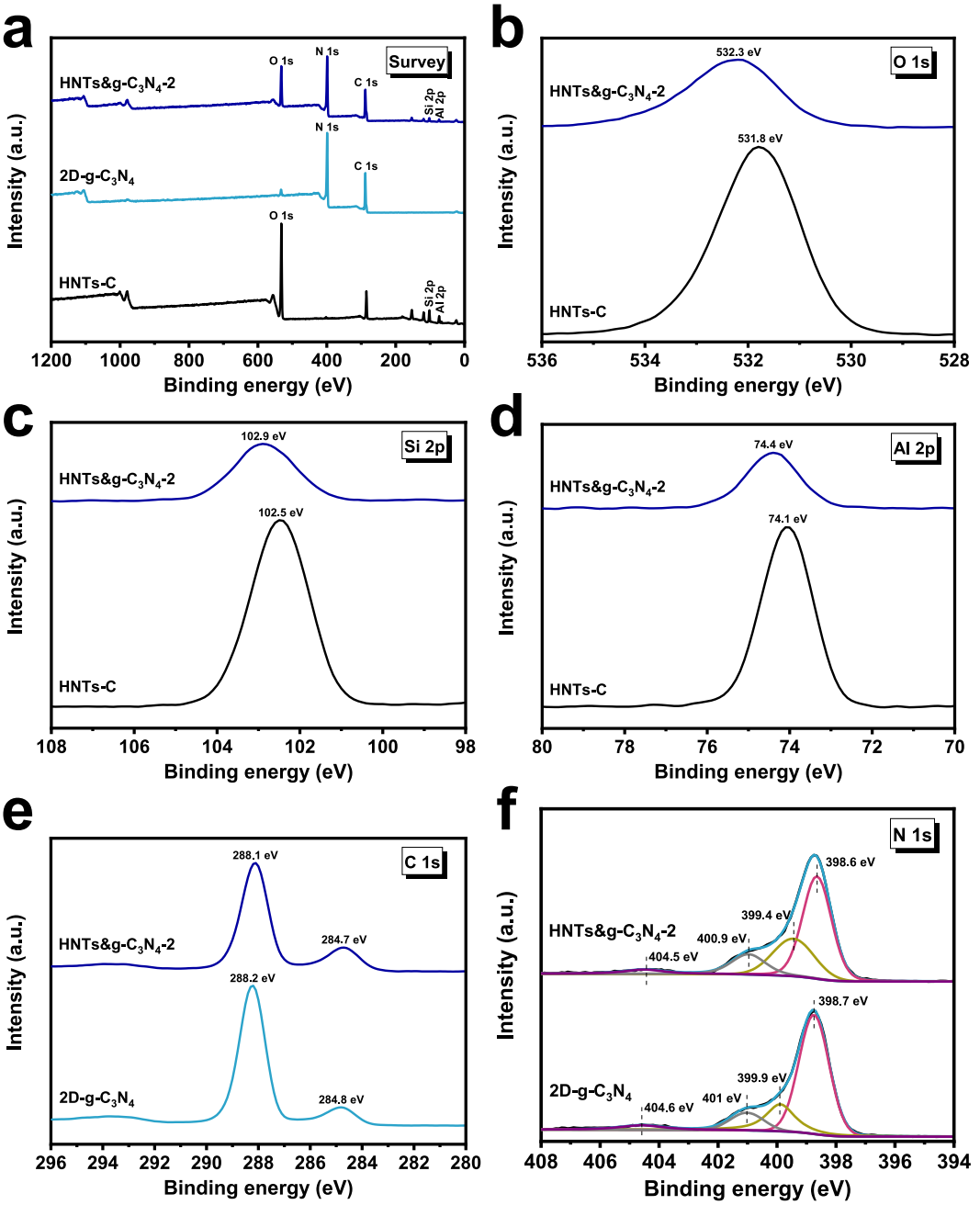

Fig. 4. XPS survey spectra (a) and high-resolution XPS spectra of O 1s (b), Si 2p (c), Al 2p (d), C 1s (e), N 1s (f) of HNTs-C, 2D-g-C_3N_4 and HNTs&g–C_3N_4–2.

between modified HNTs and debris g-C_3N_4. The detected O, Si and Al constitutes from Fig. 4b–d are coincided with the aluminosilicate component of HNTs. Concretely, the Si 2p and Al 2p XPS peaks at 102.5 and 74.1 eV are severally specified to Si–O and Al–O bonds [10,37,40]. In Fig. 4e and f, for the g-C_3N_4, the C 1s peaks are deconvoluted into two peaks, with binding energies of 284.8 and 288.2 eV, which are associated with carbon composition in the instrument and sp^2-hybridized carbon atoms of aromatic ring (N–C═N), respectively. The N 1s XPS peaks are fitted by four peaks, the sp^2-hybridized nitrogen atoms of aromatic ring (C–N═C) is located at 398.7 eV, the peaks that belonged to bridging nitrogen atoms (N−$(C)_3$) are observed at 399.9 and 401 eV, another possessed peak in 404.6 eV results from the positive charge localization in heterocycles [24,40]. After HNTs-C was anchored on 2D-g-C_3N_4, the binding signals of the above elements for HNTs&g–C_3N_4–2 are slightly switched to lower/higher positions in comparison with individual constituent, implying the successful interaction between outer surface of HNTs-C and 2D-g-C_3N_4 [15,20].

The morphologies for materials were evaluated by AFM, SEM and TEM. As observed from Fig. 5a, g-C_3N_4 after direct calcination

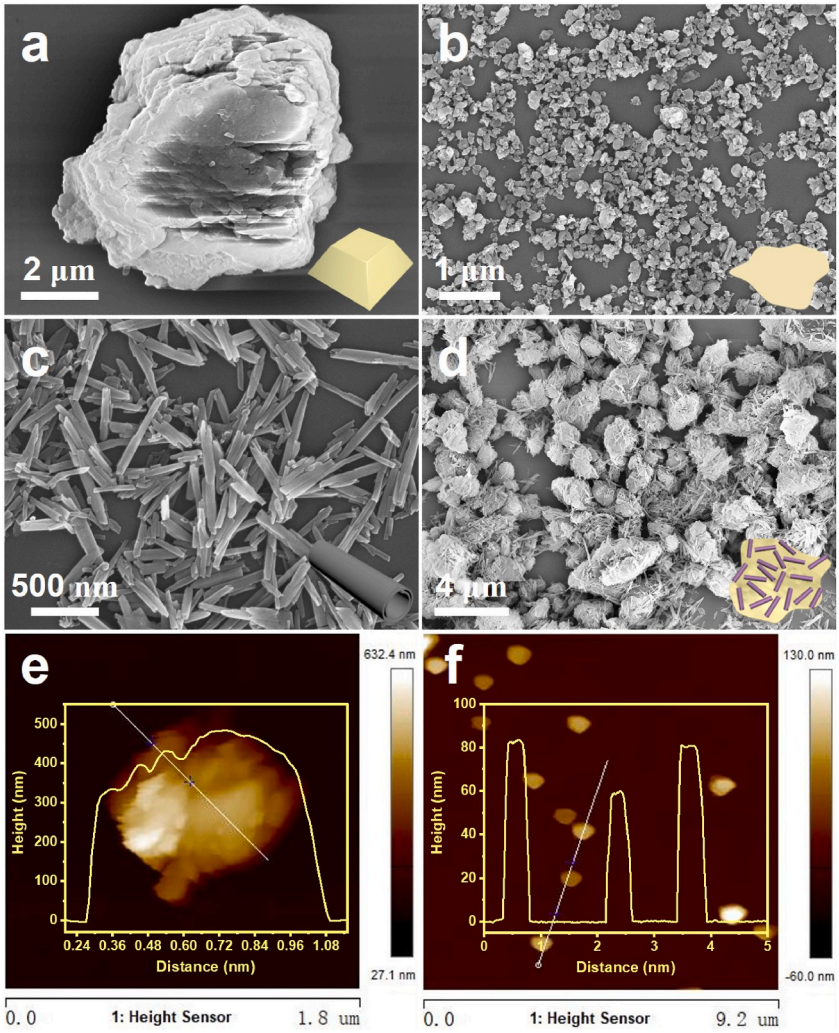

Fig. 5. SEM images and corresponding schematic diagrams of g-C_3N_4 (a), 2D-g-C_3N_4 (b), HNTs (c) and HNTs&g–C_3N_4–2 (d). AFM images and relevant height profiles (insert) of g-C_3N_4 (e) and 2D-g-C_3N_4 (f).

shows irregular chunk pattern with micron level, and it would be transformed into the nanometer-sized fragments (Fig. 5b), as is demonstrated by the change in particle size before and after cell pulverizing treatment (Fig. S5), the AFM images in Fig. 5e and f also show that bulk g-C_3N_4 has a topographic height about ~500 nm, while 2D-g-C_3N_4 displays the granules architecture with relatively smaller heights of ~80 nm. SEM and TEM patterns from Fig. 5c and Figs. S6a and b verify the smooth surface and hollow nanotube structure of HNTs with average diameters about 20–80 nm, and it can be revealed from Fig. S7 that HNTs-C could still retain its morphology after CTAB modification. Through the electrostatic self-assembly route with superficial charge divergence between 2D-g-C_3N_4 and HNTs-C, Fig. 5d and Fig. S6c show that the modified HNTs are uniformly dispersed onto debris g-C_3N_4 surface, HNTs&g–C_3N_4–2 nanomaterial which is similar to *meat floss* comprises both of this two constituents, the EDS spectrum and elemental mapping pictures demonstrate C, N, O, Si and Al elements existence within HNTs&g–C_3N_4–2, further proving the successful combination and modification of materials (Figs. S6d–g, Fig. S8, Table S2).

3.2. Photocatalytic hydrogen evolution performances

The H_2 evolution performances of the series of materials were inspected with 10 *vol*% lactic acid as sacrificial agent. In Fig. 6a and b, the 2D-g-C_3N_4 after cell pulverizing has a H_2 production quantity of 413.4 μmol g^{-1} in 4 h reaction without any co-catalysts deposition, the compound loaded by HNTs exhibits enhanced catalytic activity with the trend of first increase and then decrease, and the HNTs&g–C_3N_4–2 achieves the highest H_2 amount of 548.0 μmol g^{-1} with the rate of 137.0 μmol g^{-1} h^{-1}, it is about 3.4 times of pure g-C_3N_4, probably ascribing to quantum size and dispersion effect of 2D-g-C_3N_4 and HNTs-C that shorten photoinduced charges' migration path from bulk phase to interface of g-C_3N_4, prolonging electrons' reaction lifetime with existence of residual negative charges and hydroxyl groups localized on HNTs [41,42]. The wavelength-dependent AQE for HNTs&g–C_3N_4–2 was assessed, the AQE

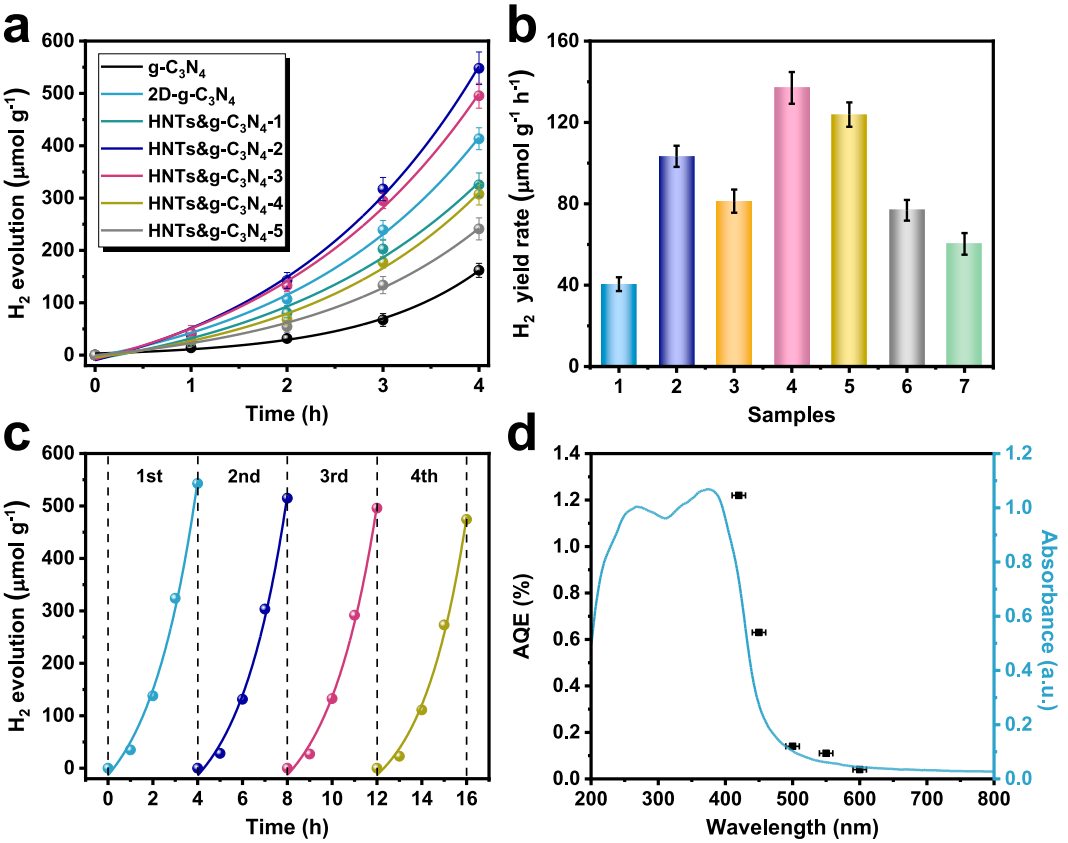

Fig. 6. Time courses of H_2 production (a) and relevant H_2 yield rates (b) of g-C_3N_4, 2D-g-C_3N_4 and the series of HNTs&g–C_3N_4–X materials (1: g-C_3N_4, 2: 2D-g-C_3N_4, 3: HNTs&g–C_3N_4–1, 4: HNTs&g–C_3N_4–2, 5: HNTs&g–C_3N_4–3, 6: HNTs&g–C_3N_4–4, 7: HNTs&g–C_3N_4–5). Cyclic tests of H_2 evolution over HNTs&g–C_3N_4–2 (c). DRS spectrum and corresponding apparent quantum efficiency of HNTs&g–C_3N_4–2 under different band-pass filters (d).

value at 420 nm band-pass filter is 1.22% and the trend is basically consistent with its DRS testing curve, tracking the characteristic absorption ability of material (Fig. 6d, Table S3).

The photochemical stability of HNTs&g–C_3N_4–2 was further conducted by the consecutive H_2 production operations under identical condition. It is plotted in Fig. 6c that despite the decrease of catalytic activity after four cyclic runs due to the wastage of photocatalyst powder during the centrifugation processes, the evolution amount of material could still be remained about 87.4% compared to fresh one, the XRD characterization and SEM image before and after cyclic measurements indicate that there is little change in crystalline phase and micromorphology of material (Fig. S9, Fig. S10), implying its favorable H_2 yield durability.

3.3. Mechanism investigations

The optical properties of g-C_3N_4, 2D-g-C_3N_4 and HNTs&g–C_3N_4–2 were examined with DRS spectra. As investigated in Fig. 7a, the absorption edge in ~460 nm is seen for g-C_3N_4 from visible light region, which should be indexed to n-π* electronic transitions from g-C_3N_4 lone pairs of nitrogen atoms [15,24], after surface loading by modified HNTs, the visible light region absorption intensity for HNTs&g–C_3N_4–2 is hardly changed, for HNTs have no absorption capacity for visible light as a kind of aluminosilicate mineral.

In order to survey the band-to-band recombination degree of photoexcited charges of materials, the g-C_3N_4, 2D-g-C_3N_4 and HNTs&g–C_3N_4–2 PL spectra at room temperature were tested. In Fig. 7b, when the excitation wavelengths are set to be 254 nm, the generated emission peaks are approximately emerged at 463 nm for all samples, that are related to band gap energy of g-C_3N_4 [41], and the signal intensity of 2D-g-C_3N_4 and HNTs&g–C_3N_4–2 spectra are remarkably weaker than g-C_3N_4, reflecting a dramatically lowered charge recombination speed, according to previous reports, the excited orbital electrons at ground state of valence band would be excited to conduct band in excited state by emitting absorbent photons [41–43], the intrinsic drawback of rapid recombination of e^--h^+ pairs has been availably surmounted through size regulation of g-C_3N_4 and the structural dispersion of HNTs.

The g-C_3N_4, 2D-g-C_3N_4 and HNTs&g–C_3N_4–2 photocurrent curves were surveyed with visible light irradiation for respective working electrodes. As shown in Fig. 7c, the current density of HNTs&g–C_3N_4–2 is higher than g-C_3N_4 and 2D-g-C_3N_4, indicating an elevated mobility of photoresponsive charge carriers. The semicircular Nyquist plots displayed in Fig. 7d disclose that the semicircle arc radius of HNTs&g–C_3N_4–2 features a smaller diameter than those of g-C_3N_4 and 2D-g-C_3N_4 whether in dark or illumination

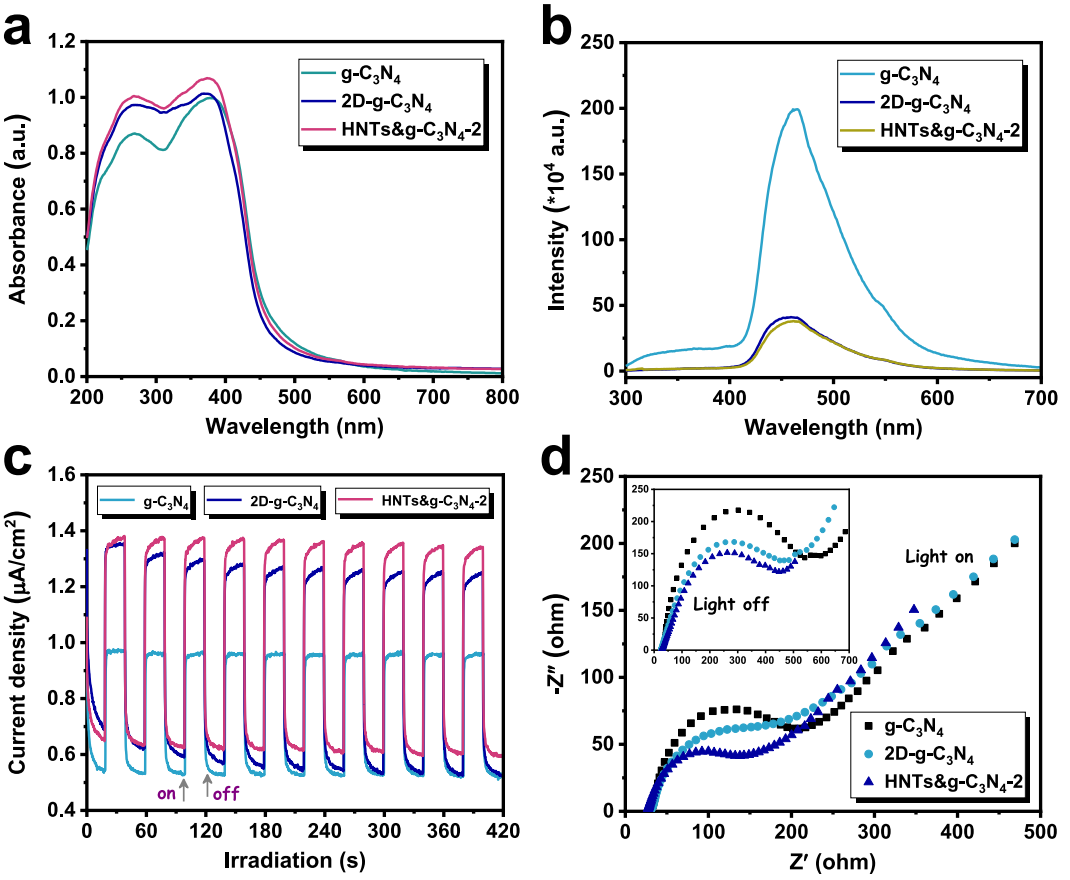

Fig. 7. DRS spectra (a), PL spectra (b), transient photocurrent curves (c) and Nyquist plots of electrochemical impedance in/without visible light illumination (d) of g-C_3N_4, 2D-g-C_3N_4 and HNTs&g–C_3N_4–2.

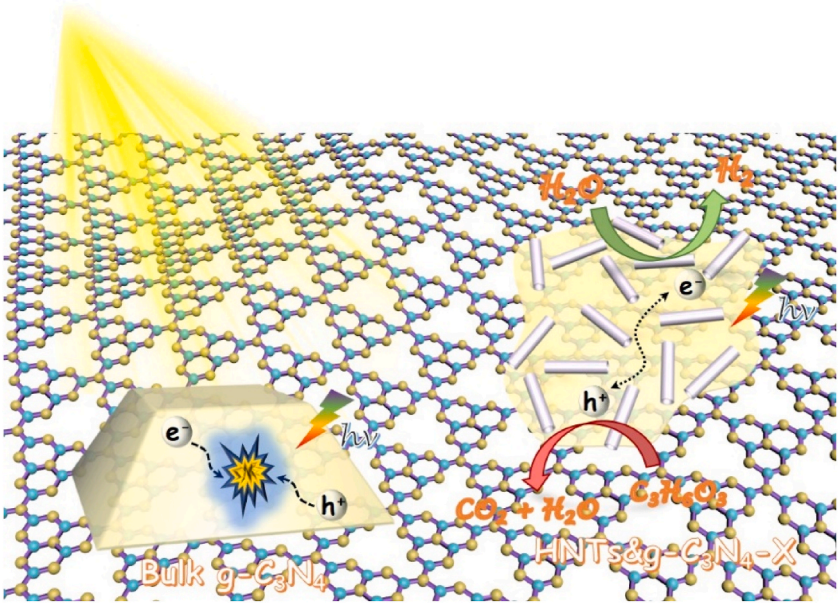

Fig. 8. Schematic mechanism of charge carriers' migration and separation over bulk g-C_3N_4 and HNTs&g–C_3N_4–X in H_2 production reaction.

condition, corresponding to a lower interfacial charge-transfer impedance value [44,45]. These photo-electrochemical measurements also verify that e^--h^+ pairs recombination degree can be restrained when g-C_3N_4 is assembled with HNTs in nanoscale dimension, which profitably facilitating the transferring rates of e^--h^+ pairs from interior to the surface, allowing enhanced specific surface area to suppress catalysts' agglomeration.

According to the characterization consequences above, the proposed H_2 evolution mechanism for materials is illustrated in Fig. 8. When under visible light ($\lambda \geq 420$ nm) illumination for bulk g-C_3N_4, the photoinduced charges are prone to be recombined with each other, leading to a poor H_2 evolution activity, while the charge recombination situation would be efficiently improved with regard to HNTs&g–C_3N_4–X nanocompound, one hand is the reduced dimension of g-C_3N_4 after cell pulverizing handle that could easily propel the free charges from bulk phase to surface of g-C_3N_4 to take part in redox reactions, where H^+ is reduced to H_2 by e^- and h^+ is preferably consumed by lactic acid to produce CO_2 and H_2O, the other aspect is the HNTs component not only trap h^+ to prolong e^- lifetime, owing to electrostatic function between remanent hydroxyl groups and negative charges of HNTs external surface, but also offer a large interfacial area to render g-C_3N_4 with good solution dispersibility, hence elevating the H_2 yield of material.

4. Conclusions

In summary, the 1D-2D HNTs&g–C_3N_4–X composite with *meat floss*-like micromorphology are successfully constructed *via* the facile cell pulverizing and electrostatic self-assembly processes. The as-obtained HNTs&g–C_3N_4–2 hybrid with 10 *wt*% HNTs loading amount has optimal photocatalytic of H_2 evolution property in a rate of 137.0 μmol g^{-1} h^{-1}, and is about 3.4-fold over bulk g-C_3N_4, which is primarily profited from the reduced morphological size of g-C_3N_4 fragments and electrons trapping function by HNTs with localized hydroxyl and negative charges on its surface, then shortening the migration path of e^--h^+ pairs from interior to g-C_3N_4 surface, and restraining recombination probability of photogenerated charges, further improving materials' H_2 evolution activity. This work affords an inorganic clay-based heteroarchitecture design on g-C_3N_4 photocatalysis enhancement with earth-abundant halloysite as target, and broadens the applications of inorganic mineral compound in the field of green energy conversion.

Author contribution statement

Sen Lin: Conceived and designed the experiment; Performed the experiments; Analyzed and interpreted the data; Wrote the paper.
Shiyong Sun: Conceived and designed the experiment; Contributed reagents, materials, analysis tools or data.
Zhengwei Li: Performed the experiments; Analyzed and interpreted the data.

Funding statement

The present work was supported by the National Natural Science Foundation of China (NSFC, grant numbers 42372056, 42061134018), the Russian Science Foundation (RSF, grant number 21-47-00019) and the Doctoral Research Foundation Project of Southwest University of Science and Technology (grant number 22zx7173).

Data availability statement

The authors do not have permission to share data.

Declaration of competing interest

The authors declare that they have no known competing financial interests or personal relationships that could have appeared to influence the work reported in this paper.

Appendix A. Supplementary data

Supplementary data to this article can be found online at https://doi.org/10.1016/j.heliyon.2023.e20520.

References

[1] H. Lu, J. Tournet, K. Dastafkan, Y. Liu, Y.H. Ng, S.K. Karuturi, C. Zhao, Z. Yin, Noble-metal-free multicomponent nanointegration for sustainable energy conversion, Chem. Rev. 121 (17) (2021) 10271–10366.
[2] Q. Zhu, Q. Xu, M. Du, X. Zeng, G. Zhong, B. Qiu, J. Zhang, Recent progress of metal sulfide photocatalysts for solar energy conversion, Adv. Mater. 34 (45) (2022) 2202929–2202954.
[3] X. Zhang, P. Yang, S.P. Jiang, Ni diffusion in vertical growth of MoS_2 nanosheets on carbon nanotubes towards highly efficient hydrogen evolution, Carbon 175 (2021) 176–186.
[4] Y. Hong, L. Yang, Y. Tian, X. Lin, E. Liu, W. Sun, Y. Liu, C. Zhu, X. Li, J. Shi, Rational design 2D/3D MoS_2/In_2O_3 composites for great boosting photocatalytic H_2 production coupled with dye degradation, J. Taiwan Inst. Chem. Eng. 146 (2023), 104862.
[5] S. Lin, S. Sun, K. Shen, D. Tan, H. Zhang, F. Dong, X. Fu, Photocatalytic microreactors based on nano TiO_2-containing clay colloidosomes, Appl. Clay Sci. 159 (2018) 42–49.

[6] S. Lin, S. Sun, K. Wang, K. Shen, B. Ma, Y. Ren, X. Fan, Bioinspired design of alcohol dehydrogenase@nano TiO_2 microreactors for sustainable cycling of NAD^+/NADH coenzyme, Nanomaterials 8 (2) (2018) 127–135.

[7] H. Zhang, B. Xu, X. Zhang, P. Yang, Raspberry-like TiO_2 hollow spheres consisting of small nanocrystals towards efficient NO removal, Environ. Sci.: Nano 9 (9) (2022) 3397–3406.

[8] L. Pan, S. Sun, Y. Chen, P. Wang, J. Wang, X. Zhang, J.J. Zou, Z.L. Wang, Advances in piezo-phototronic effect enhanced photocatalysis and photoelectrocatalysis, Adv. Energy Mater. 10 (15) (2020) 2000214–2000238.

[9] L. Cheng, Q. Xiang, Y. Liao, H. Zhang, CdS-based photocatalysts, Energy Environ. Sci. 11 (6) (2018) 1362–1391.

[10] S. Lin, S. Li, Y. Zhang, T. Ma, H. Huang, All-in-one polarized Cd/CdS/halloysite ferroelectric hybrid for exceptional photocatalytic hydrogen evolution, J. Mater. Chem. A. 9 (33) (2021) 17936–17944.

[11] C. Zeng, Y. Hu, T. Zhang, F. Dong, Y. Zhang, H. Huang, A core-satellite structured Z-scheme catalyst $Cd_{0.5}Zn_{0.5}S/BiVO_4$ for highly efficient and stable photocatalytic water splitting, J. Mater. Chem. A. 6 (35) (2018) 16932–16942.

[12] S. Tu, H. Huang, T. Zhang, Y. Zhang, Controllable synthesis of multi-responsive ferroelectric layered perovskite-like $Bi_4Ti_3O_{12}$: photocatalysis and piezoelectric-catalysis and mechanism insight, Appl. Catal., B 219 (2017) 550–562.

[13] K. Das, R. Bariki, D. Majhi, A. Mishra, K.K. Das, R. Dhiman, B.G. Mishra, Facile synthesis and application of $CdS/Bi_{20}TiO_{32}/Bi_4Ti_3O_{12}$ ternary heterostructure: a synergistic multi-heterojunction photocatalyst for enhanced endosulfan degradation and hydrogen evolution reaction, Appl. Catal., B 303 (2022) 120902–120915.

[14] Q. Zhang, S. Huang, J. Deng, D.T. Gangadharan, F. Yang, Z. Xu, G. Giorgi, M. Palummo, M. Chaker, D. Ma, Ice-assisted synthesis of black phosphorus nanosheets as a metal-free photocatalyst: 2D/2D heterostructure for broadband H_2 evolution, Adv. Funct. Mater. 29 (28) (2019) 1902486–1902495.

[15] N. Tian, Y. Zhang, X. Li, K. Xiao, X. Du, F. Dong, G.I.N. Waterhouse, T. Zhang, H. Huang, Precursor-reforming protocol to 3D mesoporous g-C_3N_4 established by ultrathin self-doped nanosheets for superior hydrogen evolution, Nano Energy 38 (2017) 72–81.

[16] C. Liu, H. Huang, L. Ye, S. Yu, N. Tian, X. Du, T. Zhang, Y. Zhang, Intermediate-mediated strategy to horn-like hollow mesoporous ultrathin g-C_3N_4 tube with spatial anisotropic charge separation for superior photocatalytic H_2 evolution, Nano Energy 41 (2017) 738–748.

[17] X. Zhang, K.M. Postolek, P. Yang, S.P. Jiang, Z-scheme WO_x/Cu-g-C_3N_4 heterojunction nanoarchitectonics with promoted charge separation and transfer towards efficient full solar-spectrum photocatalysis, J. Colloid Interface Sci. 636 (2023) 646–656.

[18] L. Wang, Y. Hong, E. Liu, Z. Wang, J. Chen, S. Yang, J. Wang, X. Lin, J. Shi, Rapid polymerization synthesizing high-crystalline g-C_3N_4 towards boosting solar photocatalytic H_2 generation, Int. J. Hydrogen Energy 45 (11) (2020) 6425–6436.

[19] K. Zhang, L. Wang, Y. Hong, X. Duan, C. Ai, L. Zhang, T. Zhang, Y. Chen, X. Lin, W. Shi, F. Guo, Iron phthalocyanine nanodots decorated ultra-thin porous carbon nitride: a combination of photocatalysis and Fenton reaction to achieve two-channel efficient tetracycline degradation, J. Alloys Compd. 966 (2023), 171580.

[20] N. Tian, H. Huang, X. Du, F. Dong, Y. Zhang, Rational nanostructure design of graphitic carbon nitride for photocatalytic applications, J. Mater. Chem. A. 7 (19) (2019) 11584–11612.

[21] B. Liu, J. Du, G. Ke, B. Jia, Y. Huang, H. He, Y. Zhou, Z. Zou, Boosting O_2 reduction and H_2O dehydrogenation kinetics: surface *N*-hydroxymethylation of g-C_3N_4 photocatalysts for the efficient production of H_2O_2, Adv. Funct. Mater. 32 (15) (2021) 2111125–2111136.

[22] X. Zhang, X.R. Zhang, P. Yang, H.S. Chen, S.P. Jiang, Black magnetic Cu-g-C_3N_4 nanosheets towards efficient photocatalytic H_2 generation and CO_2/benzene conversion, Chem. Eng. J. 450 (2022), 138030.

[23] N. Tian, H. Huang, C. Liu, F. Dong, T. Zhang, X. Du, S. Yu, Y. Zhang, *In-situ* co-pyrolysis fabrication of CeO_2/g-C_3N_4 n-n type heterojunction for synchronously promoting the photo-induced oxidation and reduction properties, J. Mater. Chem. A. 3 (33) (2015) 17120–17129.

[24] N. Tian, H. Huang, Y. He, Y. Guo, Y. Zhang, Organic-inorganic hybrid photocatalyst g-C_3N_4/Ag_2CO_3 with highly efficient visible-light-active photocatalytic activity, Colloids Surf., A. 467 (2015) 188–194.

[25] X. Zhang, P. Yang, S.P. Jiang, Ni clusters-derived 2D/2D layered $WO_x(MoS_2)$/Ni-g-C_3N_4 step-scheme heterojunctions with enhanced photo- and electro-catalytic performance, J. Power Sources 510 (2021), 230420.

[26] X. Zhang, S.P. Jiang, Layered g-C_3N_4/TiO_2 nanocomposites for efficient photocatalytic water splitting and CO_2 reduction: a review, Mater. Today Energy 23 (2022), 100904.

[27] X. Zhang, K.M. Postolek, P. Yang, Heterojunction nanoarchitectonics of WO_x/Au-g-C_3N_4 with efficient photogenerated carrier separation and transfer toward improved NO and benzene conversion, Mater, Today Adv 17 (2023), 100355.

[28] T. Song, X. Zhang, P. Yang, Interface engineering of W_2C/W_2N co-catalyst on g-C_3N_4 nanosheets for boosted H_2 evolution and 4-nitrophenol removal, Environ. Sci.: Nano 9 (5) (2022) 1888–1899.

[29] L. Chen, S. Ning, R. Liang, Y. Xia, R. Huang, G. Yan, X. Wang, Potassium doped and nitrogen defect modified graphitic carbon nitride for boosted photocatalytic hydrogen production, Int. J. Hydrogen Energy 47 (30) (2022) 14044–14052.

[30] X. Zhang, X. Zhang, P. Yang, S.P. Jiang, Layered graphitic carbon nitride: nano-heterostructures, photo/electro-chemical performance and trends, J. Nanostruct. Chem. 12 (5) (2021) 669–691.

[31] X. Hu, Z. Shu, H. Guo, J. Zhou, T. Li, Y. Tan, Z. Liao, W. Wang, Z. Zhao, Metakaolin-based nano-structuring of polymeric carbon nitride and synchronous composite construction for superior photocatalytic H_2 evolution, Appl. Clay Sci. 184 (2020) 105320–105327.

[32] B. Tahir, M. Tahir, M.G. Mohd Nawawi, Well-designed 3D/2D/2D WO_3/Bt/g-C_3N_4 Z-scheme heterojunction for tailoring photocatalytic CO_2 methanation with 2D-layered bentonite-clay as the electron moderator under visible light, Energy Fuels 34 (11) (2020) 14400–14418.

[33] Z. Jia, T. Li, Z. Zheng, J. Zhang, J. Liu, R. Li, Y. Wang, X. Zhang, Y. Wang, C. Fan, The BiOCl/diatomite composites for rapid photocatalytic degradation of ciprofloxacin: efficiency, toxicity evaluation, mechanisms and pathways, Chem. Eng. J. 380 (2020) 122422–122434.

[34] G. Dong, L. Zhao, X. Wu, M. Zhu, F. Wang, Photocatalysis removing of NO based on modified carbon nitride: the effect of celestite mineral particles, Appl. Catal., B 245 (2019) 459–468.

[35] M. Massaro, C.G. Colletti, G. Lazzara, S. Milioto, R. Noto, S. Riela, Halloysite nanotubes as support for metal-based catalysts, J. Mater. Chem. A. 5 (26) (2017) 13276–13293.

[36] M. Massaro, M. Casiello, L. D'accolti, G. Lazzara, A. Nacci, G. Nicotra, R. Noto, A. Pettignano, C. Spinella, S. Riela, One-pot synthesis of ZnO nanoparticles supported on halloysite nanotubes for catalytic applications, Appl. Clay Sci. 189 (2020) 105527–105536.

[37] S. Lin, Y. Zhang, Y. You, C. Zeng, X. Xiao, T. Ma, H. Huang, Bifunctional hydrogen production and storage on 0D-1D heterojunction of $Cd_{0.5}Zn_{0.5}S$@halloysites, Adv. Funct. Mater. 29 (39) (2019) 1903825–1903834.

[38] V.A. Vinokurov, A.V. Stavitskaya, E.V. Ivanov, P.A. Gushchin, D.V. Kozlov, A.Y. Kurenkova, P.A. Kolinko, E.A. Kozlova, Y.M. Lvov, Halloysite nanoclay based CdS formulations with high catalytic activity in hydrogen evolution reaction under visible light irradiation, ACS Sustainable Chem. Eng. 5 (12) (2017) 11316–11323.

[39] W. Ma, Y. Zhu, X. Wang, Au nanoparticles modified HNTs/g-C_3N_4/CdS composite for highly efficient CO_2 photoreduction and tetracycline degradation, J. Alloys Compd. 935 (2023) 168129–168136.

[40] M. Hojamberdiev, M.M. Khan, Z. Kadirova, K. Kawashima, K. Yubuta, K. Teshima, R. Riedel, M. Hasegawa, Synergistic effect of g-C_3N_4, $Ni(OH)_2$ and halloysite in nanocomposite photocatalyst on efficient photocatalytic hydrogen generation, Renew. Energy 138 (2019) 434–444.

[41] Y.P. Zhu, T.Z. Ren, Z.Y. Yuan, Mesoporous phosphorus-doped g-C_3N_4 nanostructured flowers with superior photocatalytic hydrogen evolution performance, ACS Appl. Mater. Interfaces 7 (30) (2015) 16850–16856.

[42] H. Huang, K. Xiao, N. Tian, F. Dong, T. Zhang, X. Du, Y. Zhang, Template-free precursor-surface-etching route to porous, thin g-C_3N_4 nanosheets for enhancing photocatalytic reduction and oxidation activity, J. Mater. Chem. A. 5 (33) (2017) 17452–17463.

[43] S. Lin, H. Huang, T. Ma, Y. Zhang, Photocatalytic oxygen evolution from water splitting, Adv. Sci. 8 (1) (2020) 2002458–2002501.
[44] S. Lin, S. Li, H. Huang, H. Yu, Y. Zhang, Synergetic piezo-photocatalytic hydrogen evolution on $Cd_xZn_{1-x}S$ solid-solution 1D nanorods, Small 18 (8) (2021) 2106420–2106430.
[45] C. Liu, Y. Zhang, F. Dong, A.H. Reshak, L. Ye, N. Pinna, C. Zeng, T. Zhang, H. Huang, Chlorine intercalation in graphitic carbon nitride for efficient photocatalysis, Appl. Catal., B 203 (2017) 465–474.